ROYAL SOCIETY OF CHEMISTRY

www.rsc.org/softmatter

Soft Matter

ARTICLE

Viscoelastic Polymer Flows and Elastic Turbulence in Three-Dimensional Porous Structures

Jonathan Mitchell,[a] Kyle Lyons,[a] Andrew M. Howe,[a,b] and Andrew Clarke[†,a]

Viscoelastic polymer solutions flowing through reservoir rocks have been found to improve oil displacement efficiency when the aqueous-phase shear-rate exceeds a critical value. A possible mechanism for this enhanced recovery is elastic turbulence that causes breakup and mobilization of trapped oil ganglia. Here, we apply nuclear magnetic resonance (NMR) pulsed field gradient (PFG) diffusion measurements in a novel way to detect increased motion of disconnected oil ganglia. The data are acquired directly from a three-dimensional (3D) opaque porous structure (sandstone) when viscoelastic fluctuations are expected to be present in the continuous phase. The measured increase in motion of trapped ganglia provides unequivocal evidence of fluctuations in the flowing phase in a fully complex 3D system. To the best of our knowledge, this work represents the first direct evidence of elastic turbulence in a realistic reservoir rock – a measurement that cannot be readily achieved by conventional laboratory methods. We support our NMR data with optical microscopy studies of fluctuating ganglia in simple two-dimensional (2D) microfluidic networks, with consistent apparent rheological behaviour of the aqueus phase, to provide conclusive evidence of elastic turbulence in the 3D structure and hence validate the proposed flow-fluctuation mechanism for enhanced oil recovery.

Introduction

Phenomena governing transport of non-Newtonian fluids in porous materials[1] are important in a wide variety of industrial and natural processes across diverse fields including biophysics,[2] geophysics,[3] and chemical engineering.[4] For most cases of liquids flowing through porous materials, the pore length-scale is small, leading to low Reynolds numbers of order $Re < 10^{-2}$ for typical flow velocities. Single-phase flows are therefore expected to be dominated by viscous forces[5] and be described by Darcy's law.[6] However, transport of multiple fluid phases is more complicated.[7] Of interest here is the displacement of one phase by a second, immiscible phase – a situation of relevance to CO_2 storage,[8] groundwater remediation, and oil recovery from subsurface reservoirs.[9] Forced displacement of oil usually proceeds by the injection of water (brine) which, after propagation of transients and shock fronts, leaves disconnected oil ganglia (regions of oil potentially spanning several pores but typically with a wide distribution of sizes) trapped in the pore structure.[10] After water flooding, typically less than 40% of the original oil in place has been produced, leaving the residual oil remaining as immobile ganglia or simply bypassed. Improved recovery is achieved through a variety of methods, depending on the oil

viscosity, liquid-liquid and liquid-solid interactions, and geophysical rock properties (porosity, permeability).[9] One enhanced oil recovery (EOR) method is inclusion of polymers in the injection water to increase the aqueous-phase viscosity and improve the mobility ratio,[9, 11, 12] thereby enabling the displacement of previously bypassed oil (e.g., due to a Saffman-Taylor instability). Additionally, several authors have noted that mobilization of trapped oil beyond that expected from the increased aqueous-phase viscosity is achieved through the use of viscoelastic polymers.[13-15] Recently, we proposed a mechanism for this additional displacement based on the presence of elastic turbulence in the aqueous phase, i.e., a flow field that varies randomly in space and time. Elastic turbulence is seen to promote breakup and mobilization of otherwise-trapped oil ganglia,[3] as long as the capillary number at the onset of elastic turbulence is lower than the capillary number required for desaturation with a Newtonian liquid.[16] High-molecular-weight flexible polymers are known to exhibit long relaxation times that lead to elastic instabilities, particularly in curvilinear flow fields.[17] This mechanistic interpretation was supported by direct imaging of multiphase flow in two-dimensional (2D) microfluidic networks (micromodels) where elastic turbulence in the aqueous phase, observed through particle tracking, was shown to coincide with trapped oil ganglia fluctuations, breakup, and displacement.[3] In the same work, EOR was demonstrated in three-dimensional (3D) sandstone rock plugs under consistent flow conditions, and the same mechanism was inferred for this recovery process. We used low-field nuclear magnetic resonance (NMR) to monitor the oil saturation (the volume

a. Schlumberger Gould Research, High Cross, Madingley Road, Cambridge CB3 0EL, UK.
b. Current address: BP Institute for Multiphase Flow, Madingley Road, Cambridge CB3 0EZ
† Author to whom correspondence should be sent. E-mail: AClarke3@slb.com. Tel: +44 (0)1223 325222.

fraction of oil within the pore space) in these rock plugs.[18] However, we were not able to visualize elastic turbulence or ganglia fluctuations directly within the macroscopic opaque 3D pore structures, and thus their presence could only be inferred from the increase in apparent viscosity that commenced at flow rates expected to coincide with the onset of fluctuations. Here, we use NMR pulsed-field-gradient (PFG) diffusion measurements in a novel way to probe the motion of trapped oil ganglia under flow conditions expected to induce elastic turbulence in the continuous aqueous phase and within an opaque macroscopic (57cm^3) cylinder of sandstone rock. NMR diffusion measurements are sensitive to root-mean-square (RMS) displacements over a defined observation time t_Δ,[19] and so fluctuations of oil ganglia that exceed the average diffusion path-length of the oil molecules will manifest as an increased apparent diffusion coefficient D_{app}. The estimated increase in oil mobility observed through the diffusion measurements is compared to drop menisci fluctuations observed in 2D microfluidic networks by optical microscopy under comparable flow conditions. In 2D such fluctuations have been previously reported.[3] In this way we unequivocally demonstrate the existence of spatial fluctuations of trapped oil ganglia in 3D. Accordingly, through this novel approach we connect the observations made in model microfluidic systems to a flow in a fully complex macroscopic 3D porous network.

Experimental

Samples

Partially hydrolysed polyacrylamides (HPAMs) with molecular weights in the range 3.5 to 35 MDa have proven popular for EOR projects. Studies of solutions of these polymers under flow in porous media and by conventional rheometry have shown that the onset of elastic turbulence is independent of polymer concentration over the low-shear viscosity range of 20 mPa s to 20 Pa s.[16, 20] Additionally, the onset of elastic turbulence – characterized by a change from shear thinning to thickening in porous flow – depends on molecular weight squared.[16] The onset of an increase in apparent viscosity has been described by a polymer solution characteristic time λ_{PM} derived from cone-and-plate rheometry (where the subscript PM refers to Pakdel-McKinley to distinguish this parameter from other characteristic times)[21] that allows us to define a Weissenberg number as $\mathrm{Wi} = \lambda_{PM}\dot{\gamma}$, where $\dot{\gamma}$ is the shear rate defined as

$$\dot{\gamma} = \frac{Q}{S_w A \sqrt{k\phi}}, \tag{1}$$

for flow in porous media such that Q is the imposed volumetric flow rate, A is the total cross-sectional area available to flow, S_w is the aqueous-phase saturation (fraction of pore volume occupied by the specified fluid), ϕ is the porosity, and k is the permeability. Accordingly, Wi becomes useful for estimating the flow conditions necessary to induce elastic instabilities

when flowing polymer solutions through different geometries, such as microfluidic networks and rock plugs.

Low-salinity (74mM) D$_2$O brine was used in all studies to eliminate any proton NMR signal from the aqueous phase and allow unambiguous detection of the oil. The same formulations were used in the microfluidic experiments for consistency. Polymer solutions were prepared in this brine with 18 to 20 MDa HPAM (3630S, SNF Floerger), or xanthan (International Drilling Fluids IDF), at a concentration of 0.12%w/v; this concentration provided a similar low-shear viscosity of $\eta(0) \approx 120\,\mathrm{mPa\,s}$ for both polymer solutions.[16] The oil was a viscosity standard (S20, PSL-Rheotek) with η = 34 mPa s at 20°C. Bentheimer sandstone rock samples (core plugs) were used for all coreflood experiments. These were cored from a block of quarried outcrop rock, trimmed, and dried overnight at 60°C in a vacuum oven. The porosity ϕ (helium) and gas permeability k (nitrogen at a mean pore pressure of 1.5 psi) of the dry plugs were determined, and found to be consistent at ϕ = 0.23 and k = 2600 mD. The plugs were cylindrical with dimensions 50 mm × 38 mm (length × diameter). For these plugs, the pore volume of 1 PV ≡ 13 cm^3 was typical. The sandstone grains were water-wet such that the rock was able to spontaneously imbibe water.

Rheology of the liquids was assessed using both shear rheometry and flow in the porous medium.[3] These data are shown in Fig. 1. Further mode detailed rheological data is shown in the appendix. The simple shear measurements were made at 20°C with a Malvern Gemini NanoHR rheometer using a Mooney Ewart (C2.3/26) measuring geometry. The similarity in the flow curves for the xanthan and HPAM solutions indicates that these liquids have closely similar behaviour in shear. Also, the apparent shear behaviour of the HPAM solution is consistent when flowing in the Bentheimer rock and the microfluidic network; in each porous system the HPAM solution exhibits apparent flow thickening above about 10 to 15 s^{-1}. Significantly, xanthan does not show the same thickening behaviour when flowing in porous media (data not included for clarity), and the apparent flow curve closely overlays the shear rheometry data.[3] The apparent thickening observed for HPAM is associated with the onset of elastic turbulence in the microfluidic device and was therefore previously assumed to coincide with the onset of elastic turbulence in the rock.[3]
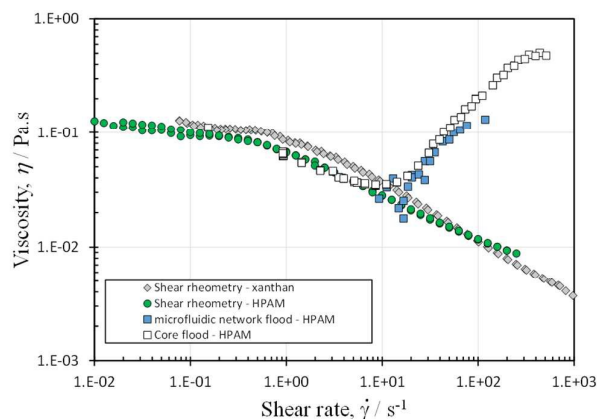
Figure 1. Measured rheology of the solutions used in this study. Shear rheometry of 0.12%w/v 18 to 20 MDa HPAM and 0.127%w/v xanthan are shown. Also shown are the apparent viscosity of the HPAM solution derived from flow measurement in Bentheimer (coreflood) and in the microfluidic network.

Coreflood

A Bentheimer plug was vacuum saturated with brine before being loaded into a NMR-compatible core holder. Oil was pumped through the plug at a volumetric flow rate of $Q = 0.167$ cm^3 s^{-1}, providing an initial oil saturation (volume fraction of oil in pore space) of typically $S_{oi} = 0.95$. Brine was then injected into the plug at $Q = 0.002$ cm^3 s^{-1} to provide a residual oil saturation $S_{or} = 0.29$ to water flooding (determined by calibrated NMR volumetrics). NMR-diffusion data were acquired at various intervals during this desaturation process (oil displacement from rock). The ganglia fluctuation measurements then proceeded by the following steps: (i) 10 PV of aqueous phase (brine, HPAM solution, or xanthan solution) was injected at the required flow rate to achieve a new residual oil saturation; (ii) flow of the aqueous phase continued and NMR-diffusion data were acquired; (iii) the flow was halted and a second NMR-diffusion measurement was made under static conditions at the same oil saturation as the previous (flowing) measurement. A fresh sandstone plug was used for each aqueous-phase flood to avoid complications of polymer interactions and exchange at pore surfaces. Brine and xanthan solutions were injected at $Q = 0.083$ cm^3 s^{-1}; the HPAM polymer solution was injected at increasing flow rates from $Q = 0.017$ to 0.167 cm^3 s^{-1}. Oil saturations were determined by comparing the total signal measured in the absence of flow to a bulk oil sample of known mass. Differential pressures were recorded across the plug throughout the floods. The polymer solution flow rate was *increased* sequentially to provide the maximum oil saturation, i.e., maximum NMR signal at each flow rate, equivalent to a capillary desaturation experiment.[18] A consequence of this experimental design is that the size distribution of the trapped oil ganglia is expected to vary with flow rate. The NMR measurement is sensitive to the ensemble average of all oil in the rock, so the change in saturation is expected only to influence the sensitivity of the measurement.

NMR PFG Diffusion

An Oxford Instruments benchtop "Rock Core Analyzer" permanent magnet was used, operating at a resonance frequency of 12.9 MHz for ^{1}H. This magnet has a vertical-bore solenoid resonator providing typical 90° and 180° radio frequency (rf) pulse durations of $t_{90} = 15$ μs and $t_{180} = 30$ μs, respectively. Slab-format gradient coils provided magnetic field gradients up to $g_{max} = 0.25$ T m^{-1} (x and y) or $g_{max} = 0.45$ T m^{-1} (z); the stronger gradient available on the z-axis was used for the PFG-diffusion measurements and provided sensitivity to motion perpendicular to the imposed flow direction in y. Spoiler gradients were applied on the x and y axes to dephase any signal from unwanted coherent spins. Diffusion measurements were made using the standard bipolar stimulated-echo pulse sequence (also known as the Cotts-13 interval pulse sequence).[22] This particular PFG sequence was chosen to reduce the influence of internal gradients on the diffusion measurement.[23] Acquisition parameters were chosen to maximize the diffusion encoding time for the oil while maintaining a useful signal-to-noise ratio (SNR). The bulk oil had a log-mean longitudinal relaxation time of $T_{1lm} = 300$ ms, so the observation time was fixed at $t_\Delta = 250$ ms. Trapezoidal gradient pulses were used with a total pulse duration $t_\delta = 5$ ms and a ramp time of $t_\varepsilon = 0.5$ ms; the stimulated echo time was $2\tau_{ste} = 8$ ms, and the gradient amplitude was ramped linearly from $g_z = 0.014$ to 0.440 T m^{-1} in 20 steps. A recycle delay of 5 s was allowed between scans, and 16 repeat scans were summed to accommodate the rf phase cycle and improve SNR. The total acquisition time for each diffusion measurement was 30 min. Following the notation of Tanner,[24] the magnetization decay is given by[25]

$$\frac{m(g)}{m(0)} = \exp\left\{-\gamma^2 g^2 D\left[t_\delta^2\left(t_\Delta - \frac{t_\delta}{3}\right) + \frac{t_\varepsilon^3}{30} - \frac{t_\delta t_\varepsilon^2}{6}\right]\right\}, \qquad (2)$$

where γ is the ^{1}H gyromagnetic ratio, and D is the diffusion coefficient. For the purpose of fitting these data, we simplify the exponent in eq. (2) to $-bD$, where the b-factor is determined by the experimental parameters.

Micromodels

The microfluidic network (manufactured by Epigem Ltd) was a simple 2D representation of a porous structure. Square nodes (pores) of width 200 μm were placed on a regular grid, connected by channels (pore throats) with a randomized width about 75 μm. The channels were aligned at 45° to the imposed flow direction. The network is supplied with SU8 internal surfaces, which were modified to be predominantly water-wet.[26] The microfluidic network was initially filled with oil and then desaturated to a residual oil saturation, i.e., where no further oil displacement occurred, by injecting brine at $Q = 1.7\times10^{-4}$ cm^3 s^{-1}. HPAM polymer solution was subsequently injected at *decreasing* flow rates of $Q = 2\times10^{-3}$ to 1.2×10^{-4} cm^3 s^{-1}. By decreasing the flow rate (cf. *increasing* flow rate in the NMR coreflood), the same trapped oil configuration could be monitored throughout as no further desaturation occurred. Note that in these experiments, the oil is trapped as single drops within a pore, thus for the micromodel data we refer to

ARTICLE   Journal Name

drops rather than ganglia. At each flow rate, an image sequence was acquired. A FireWire camera (AVT Pike-505C) was used to image trapped oil drops (at approximately 20 fps), and image-processing edge-detection algorithms were used to measure the drop fluctuations. For each drop, 180 radial lines were chosen and the drop edge detected along each line. The resulting edge points were used to determine the centre of mass of the drop, i.e., the drop position in both the cross-flow (z) and in-flow (y) directions. Note that the drops are observed to span the thickness (x) of the microfluidic device for all drops chosen for measurement. The power spectral density (PSD) of the z position calculated using an autoregressive algorithm is plotted in Fig. 2. Insets are a time trace from which the PSD is calculated and an image from the sequence.

In the fluctuation analysis procedure, only the displacement of the drop centre of mass was followed (drop deformation was not assessed). A drop displacement amplitude equivalent to that obtained in the NMR measurements was calculated as 6σ, with σ the standard deviation of the centre of mass position in the cross-flow direction, z, as in the NMR experiments. The factor 6 approximates the full amplitude of displacement from the RMS value. The equivalent of a mass average over all drops in the image was generated by taking the area average displacements as

$$\langle d \rangle = \frac{\sum_{n=1}^{N-1} a(n)d(n)}{\sum_{n=1}^{N-1} a(n)}, \qquad (3)$$

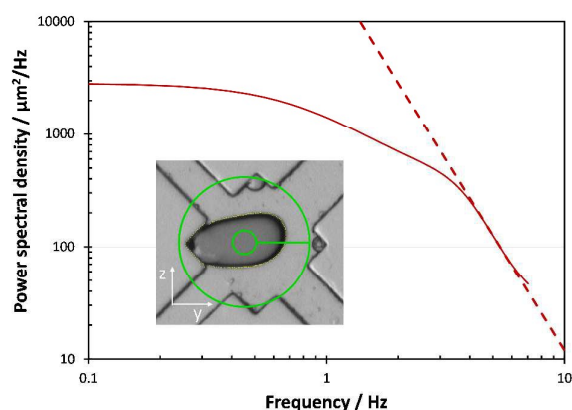where $a(n)$ is the area of the nth drop and $d(n)$ the displacement of the nth drop.

Figure 2. Power spectral density of centre-of-mass fluctuations of a trapped oil drop (solid line). Also plotted (dashed) is a line with slope -3.4. This power-law cutoff is comparable with that observed by other workers for elastic turbulence velocity fluctuation spectra.[27] Inset (bottom left) is the first of the sequence of images from which the time trace is extracted.

Results

Coreflood

The oil saturation in the Bentheimer plugs, subsequent to the initial desaturation using brine and as a function of interstitial aqueous-phase flow rate, is shown in Fig. 3. The oil saturation was not reduced significantly by injecting brine at a higher rate. In previous studies we have seen that interstitial brine velocities obtained with a flow rate of $Q > 0.13$ cm^3 s^{-1} are required to induce additional desaturation.[18] The xanthan polymer solution was not able to reduce the oil saturation much beyond that achieved by brine as the solution is flow thinning at these relatively high interstitial velocities (the NMR measurement was made at an equivalent shear rate of 131 s^{-1}). However, the viscoelastic HPAM solution was able to achieve a significant reduction in oil saturation at similar interstitial flow velocities. An increase in $\Delta P/Q$ across the plug with increasing flow rate indicated that the HPAM polymer solution was exhibiting apparent flow thickening, as expected from Fig.1.

Examples of the oil-diffusion data obtained while flowing HPAM polymer solution are shown in Fig. 4. The equivalent diffusion data, obtained at the same saturation state in the absence of flow, are also shown for comparison. The *static* data were fitted by a *mono*-exponential decay function of the form $m(b) = m(0)\exp\{-bD_0\}$, where $D_0 = 61.5$ µm^2 s^{-1} $\pm$ 20 µm^2 s^{-1} is the diffusion coefficient of the bulk oil. As the oil contains a mixture of hydrocarbon chains, a mono-exponential function is not expected to fit the data precisely, but our interpretation does not require more elaborate fitting, such as a multi-exponential inversion.[28] Regardless of the saturation state, a diffusion coefficient consistent with the bulk oil value was obtained, indicating that the diffusion measurement was not sensitive to ganglia size through restricted diffusion[29] on the time-scale of the measurement.
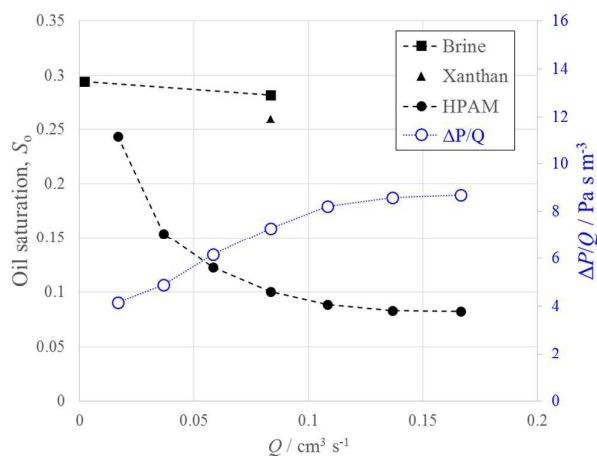

Figure 3. Oil saturation as a function of aqueous-phase flow rate for brine, xanthan (pseudoplastic) polymer solution, or HPAM 3630S (viscoelastic) polymer solution. The oil saturation was determined from the NMR signal amplitude. The pressure gradient imposed by the flowing HPAM polymer solution is included (right-hand axis).

The oil-diffusion data acquired during flow of the HPAM polymer solution could not be fitted with a mono-exponential decay, except at the lowest flow rate studied ($Q = 0.017$ cm^3 s^{-1}). Therefore, data acquired *during flow* of HPAM solution

were fitted with a *bi*-exponential function of the form: $m(b) = m_a(0)\exp\{-bD_{app}\} + m_b(0)\exp\{-bD_0\}$ where $m_a(0) + m_b(0) = m(0)$. To improve the robustness of the bi-exponential fits, the slow-diffusion coefficient was fixed at the bulk oil value of $D_0 = 61.5$ μm^2 s^{-1}, and only the amplitude m_b allowed to vary. Both the amplitude and diffusion coefficient were allowed to vary for the fast-diffusion component. The fast-diffusion coefficient increased with increasing flow rate up to $Q \approx 0.14$ cm^3 s^{-1}, where the fast-diffusion coefficient appeared to reach a plateau at approximately $D_{app} \approx 520$ μm^2 s^{-1}.

In contrast to the flowing HPAM solutions, all the data acquired during flow of brine and of xanthan polymer solution were well fitted by a mono-exponential function. The apparent diffusion coefficients obtained from all the experiments are combined in Fig. 5. At an aqueous-phase flow rate above 0.02 cm^3 s^{-1} for the viscoelastic HPAM polymer solution, the fast-diffusion component observed in the data increases with increasing flow rate and appears to saturate above about 0.14 cm^3 s^{-1}. The fast diffusion coefficient had an amplitude corresponding to approximately 25% of the total signal at all flow rates, implying the fraction of oil in ganglia able to fluctuate was relatively constant regardless of saturation.
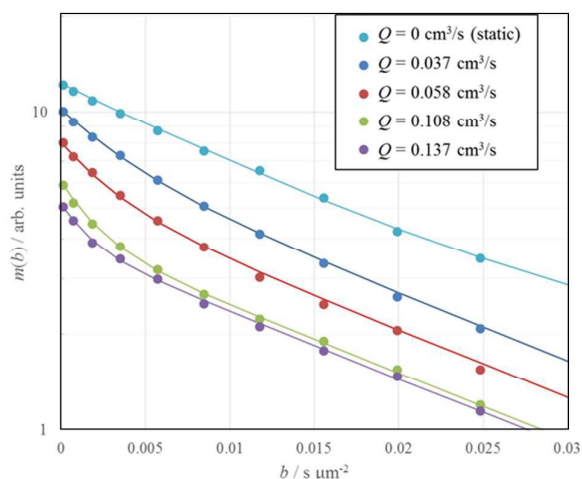

Figure 4. Diffusive attenuation data for oil during flow of HPAM 3630S polymer solution over a range of flow rates. The data acquired during flow were fitted with a bi-exponential decay function (solid lines) with one component fixed at the bulk (static) value.

In these experiments, since during each measurement no oil was collected from the rock it was assumed that the oil was trapped and that no further desaturation occurred. However, to confirm that transport of oil would not have a significant influence on the measured diffusion coefficients, diffusion data were obtained during the initial brine desaturation stage, see Fig. 6. Despite the fact that a significant fraction of the oil is flowing during the initial desaturation stages, the observed diffusion coefficients (measured perpendicular to the direction of imposed flow) are not greatly increased above the bulk oil diffusion coefficient. Therefore, even if some mobilization of

oil occurred during the diffusion measurements (Fig. 5), we do not expect any significant contribution to the diffusion coefficients from flowing oil.
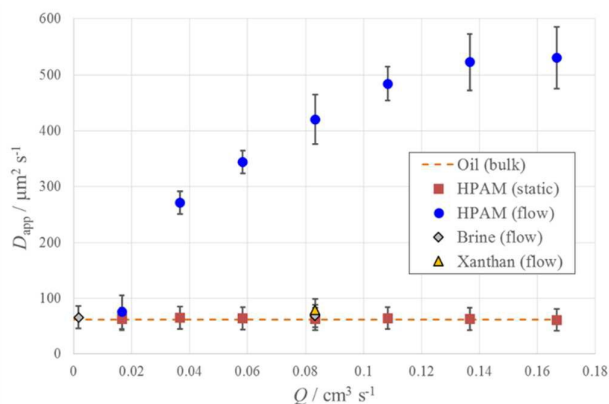

Figure 5. Apparent oil diffusion coefficients as a function of aqueous-phase flow rate for brine, xanthan polymer solution, and HPAM 3630S polymer solution. For the HPAM (flow) experiments, two diffusion coefficients were obtained for $Q >$ 0.02 cm^3 s^{-1}; only the fast-diffusion coefficients are shown for clarity. The slow-diffusion coefficients were consistent with the values obtained under static (no flow) conditions. The maximum Reynolds number explored was, $Re < 10^{-2}$.
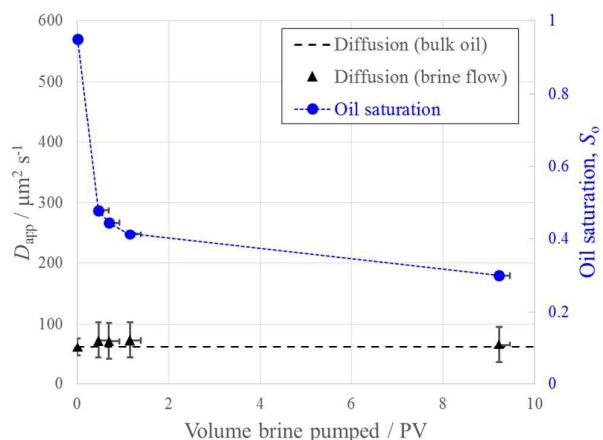

Figure 6. Diffusion coefficients of oil determined during desaturation by brine flowing at $Q = 0.037$ cm^3 s^{-1} (triangles, left-hand axis). The bulk oil diffusion coefficient is indicated by the dashed horizontal line. Also shown are the approximate saturation states (circles, right-hand axis; the dotted line is included to guide the eye) at which the diffusion data were acquired. The horizontal error bars correspond to the volume of brine injected during each diffusion measurement.

The NMR diffusion measurement implicitly assumes the oil molecules are undergoing 3D motion. To compare the NMR data to ganglia meniscus displacements observed in the microfluidic device, we extract a 1D root-mean-squared displacement using the Einstein equation $\sqrt{\langle z^2 \rangle} = \sqrt{2(D_{app} - D_0)t_\Delta}$. We subtract the diffusion term corresponding to random motion in the bulk oil, equivalent to $\sqrt{\langle z_0^2 \rangle}$ = 5.5 μm. For example, at $Q = 0.083$ cm^3 s^{-1}, the apparent diffusion coefficient corresponds to a 1D displacement of $\sqrt{\langle z^2 \rangle}$ = 13.4 μm over t_Δ = 250 ms observation time. At the same flow rate, brine and xanthan

polymer solution induce a maximum displacement of $\sqrt{\langle z^2 \rangle}$ = 3.0 µm, comparable to $\sqrt{\langle z_0^2 \rangle}$ in bulk oil. Note that the NMR processing implicitly assumes a random walk in 3D (even though the diffusion measurements were made on the z-axis) whereas the motion of the fluctuating ganglia is constrained in space. We consider the length-scale calculated from the diffusion coefficient to represent the full range of motion of the ganglia from its mean position, rather than an RMS displacement. Accordingly, we compare this length to the maximum displacement of ganglia menisci observed in the microfluidic device.

Microfluidic networks

Experiments to assess the amplitude of ganglia fluctuations in the microfluidic devices followed a similar protocol to that employed in the coreflood experiments. Here we image just a few trapped oil drops and therefore do not have full statistical averaging of the fluctuation data. We therefore choose to image the same (few) drops over a range of flow rates that map directly to the interstitial velocities observed in the core experiment. An initial brine flood brought the system to a residual oil saturation. We then flowed the polymer solution at the maximum flow rate used in the experiment and sought a region with a few trapped oil drops. Using this flow sequence, we are able to follow the same four droplets (unchanged in average position and volume) at each flow rate. We measured the oil drop centre of mass fluctuation amplitude for each of four drops within the image over a range of flow rates. The resulting data are shown in Fig. 7.

To directly compare the data shown in Fig. 5 (fast diffusion coefficient in the rock by NMR) with that shown in Fig. 7 (microfluidic network), we non-dimensionalise the abscissa by calculating an M number,[21]

$$M = \sqrt{\mathrm{WiDe}} = \lambda_{PM} \dot{\gamma} \left(\frac{a}{L} \right)^{1/2}, \qquad (4)$$

where De is the Deborah number, a is a shear length-scale, and L is a radius of streamline curvature. For our sandstone rock we estimate $a/L \approx 0.27$,[30] whereas for the microfluidic device we estimate $a/L \approx 0.21$ based on the channel geometry. The Pakdel-McKinley relaxation time for the HPAM solution used here is $\lambda_{PM} = 0.197$ s.[16] The resulting direct comparison is given in Fig. 8.
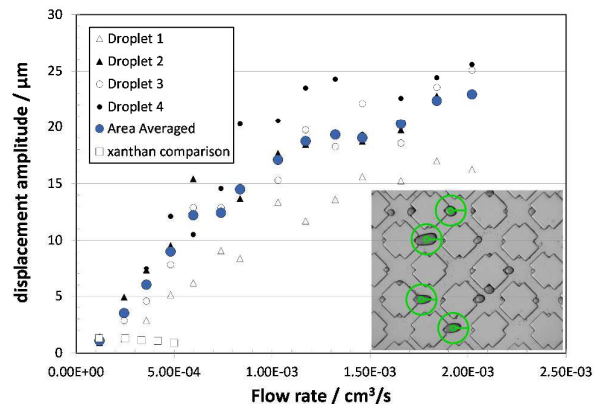

Figure 7. Measured fluctuation amplitude as a function of flow rate within the microfluidic device. Data for individual drops are plotted as small symbols (black/white circles/triangles), and the area-averaged value for all four drops as a large blue circle. Inset is an image from the sequence of fluctuating drops. The green circles indicate the radial search area for each drop. The fluctuation amplitude for a single large xanthan drop is plotted as squares; the non-zero value is due to the influence of pixel noise in the image sequence.

Discussion

The data in Fig. 8, for both the rock core measurement and the microfluidic measurement, show an increased ganglia movement above $M \approx 3$. This increase correlates with the increase in apparent viscosity observed in the single-phase coreflood experiments, see Fig. 8. Hence we directly associate the increased displacement of oil in the rock with the onset of meniscus fluctuations in the microfluidic network and the onset of apparent shear-thickening. The NMR-diffusion measurement is sensitive to any molecular motion, and as such is sensitive to coherent advective flow. The NMR measurements therefore reveal that there is a significant increase in movement of trapped oil perpendicular to the direction of average aqueous-phase flow when the aqueous solution contains a sufficiently viscoelastic polymer and the apparent aqueous-phase shear rate exceeds a critical threshold. This movement is absent during flow of a comparable shear-thinning fluid (xanthan) and for the Newtonian brine. The implication is that elastic turbulence is present in the 3D porous medium for viscoelastic solutions under suitable flow conditions.

The absolute magnitude of the oil displacements in the two measurements differ above $M \approx 10$. However, there are a number of distinctions between the two measurements that will lead to absolute changes in magnitude. These include: (i) a change in channel length-scale; (ii) the channel network dimensionality; (iii) the rock ganglia vs microfluidic drop size distribution; (iv) the geometry and configuration of trapped ganglia / drops; and (v) the average ganglia / drop size, i.e., drops in the microfluidic network were small and of fixed volume (determined by the highest flow rate) whereas ganglia size in the NMR experiment varied with flow rate with an expected decrease in average size as flow rate increased.[10] Oil ganglia in the rock may extend through multiple pores,

whereas the drops in the microfluidic network each existed in a single pore.[10, 31] Furthermore, the pore size in the rock may be expected to restrict the maximum amplitude of ganglia fluctuations, leading to the observed plateau in displacement in Fig. 8 of $\sqrt{\langle z^2 \rangle} \approx 15$ μm, where the larger pores of the microfluidic device permit a greater amplitude of fluctuation. Notwithstanding, the comparison between the two sets of data is remarkable and demonstrates that trapped oil-phase fluctuations observed in microfluidic networks are also present in the complex 3D rock structure.
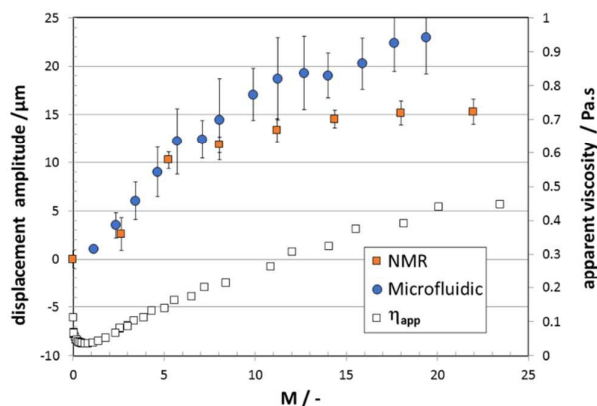

Figure 8. Comparison of RMS 1D displacement of oil measured in a rock (NMR) and in a microfluidic network, plotted against M derived using eq. (4). Overlaid for comparison are the apparent viscosity data for single-phase flow of HPAM solution in Bentheimer, reproduced from Fig. 1.

A further concern is that, within each trapped oil ganglion or drop, recirculating flows may exist driven by shear stresses induced by the flowing aqueous phase. Such recirculating flows will give rise to convective currents that result in additional signal attenuation in the NMR measurement, i.e., enhanced apparent diffusion coefficient. We address this concern in two ways. First, we flowed solutions that do not cause ganglia fluctuations (xanthan, brine) yet would induce recirculating flows in trapped ganglia. Second, we performed two-phase finite-elements calculations (Comsol). Apparent diffusion data for oil in the presence of flowing xanthan and brine solutions are included in Fig. 5, where no fluctuations are expected. Experimentally, a small increase in the apparent diffusion coefficient is observed for each of xanthan and brine, but is only on the order of 10 μm^2 s^{-1} larger than the static case. The two-phase finite-element calculations demonstrated that, for the range of materials and flow rates used, the expected amplitude of convective currents would correspond to an enhancement in measured diffusion coefficient equivalent to approximately one-tenth that of the diffusion coefficient of bulk oil. Therefore, the experimentally observed increase in apparent diffusion coefficient is comparable to that predicted by simulation, suggesting that flow-driven convection within the trapped oil ganglia is not a significant factor in our interpretation.

Conclusions

We have presented NMR diffusion data that demonstrate fluctuations of trapped oil ganglia in a macroscopic 3D porous medium (sandstone) when the flowing aqueous phase exhibits elastic turbulence. To the best of our Knowledge, this work represents the first direct observation of elastic turbulence in a fully complex 3D structure. Furthermore, we are not aware of any other laboratory technique able to probe these motions *in situ* for flow through an opaque porous medium.

The diffusion measurements in the 3D rock were supported by visualisation of trapped oil drops in a 2D microfluidic network. Onset of elastic turbulence was observed in the rock as an increase in the apparent diffusion coefficient, and in the microfluidic device as motion of the oil drop menisci. When compared via a dimensionless flow parameter, the onset of elastic turbulence in the 2D and 3D networks coincided. Surprisingly, the amplitude of fluctuations was also found to be similar in both geometries, whilst the variances were reasonably explained by geometric differences between the 2D and 3D networks.

Overall, this work demonstrates directly that trapped-phase meniscus fluctuations exist in complex 3D pore structures when solutions of very high molecular weight viscoelastic polymer are flowing sufficiently quickly (but with *Re*«1). Such trapped-phase meniscus fluctuations are driven by the presence of elastic turbulence in the aqueous phase.

Acknowledgements

Appendix

In this appendix we consider and compare the relative viscoelastic properties in shear flow of the HPAM and xanthan solutions used in this study.

Carreau-Yasuda fits to the data in Fig. 1 of the main text yield relaxation times describing the onset of shear thinning to be λ_{CY} = 2.5 and 0.9 s for the HPAM and xanthan, respectively. Further, Figure A-1 shows low-amplitude oscillatory shear moduli. The linear viscoelastic relaxation time from an extrapolation in the data to higher frequency is approximately 0.25 s for HPAM and 0.09 s for xanthan. Thus the HPAM and xanthan solutions exhibit comparable characteristic timescales in these experiments.
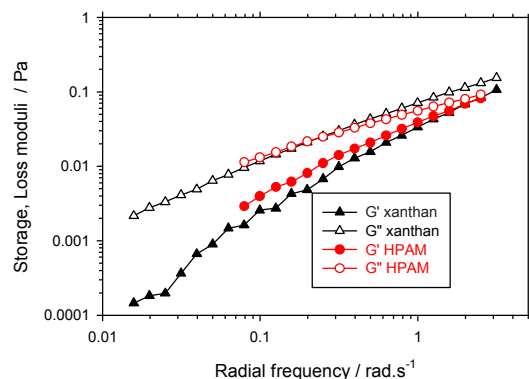
ARTICLE

Journal Name

Figure A-1 Storage (unfilled) and loss (filled) moduli as a function of radial frequency for 0.13wt% HPAM (circles) and 0.13wt% xanthan (triangles) in 74mM brine. The extrapolated relaxation time for the xanthan solution is ≈0.09s and for the HPAM solution ≈0.25s.

Further to these standard rheological measurements, we also carried out measurements in a 4°, 40 mm diameter cone-plate geometry in order that the first normal stress difference N1 could be measured. In these latter experiments, shown below in Figures A-2 and A-3, the shear stress σ was held constant for 100 s at a series of logarithmically increasing values and the "instantaneous viscosity" recorded each second. Mean values of the instantaneous viscosity and the ratio $N1/\sigma$ (a measure of the viscoelasticity) are presented as a function of shear rate. The values of viscosity and $N1/\sigma$ averaged over the period 51-100 s at each stress (i.e. during the plateau of viscosity at each stress) are plotted as a function of shear-rate in Figure A-3 to enable closer comparison between the polymer solutions. In figure A-3, the viscosity of the HPAM sample shows a sudden thickening from approximately 75 s^{-1} where the viscosity minimum is 12 mPa.s. The thickening is interpreted as the onset of elastic fluctuations in this geometry.[21] The xanthan solution viscosity continues thinning to ≈ 500 s^{-1} (minimum viscosity ≈ 5-6 mPa.s) before plateauing and then gradually increasing. The thickening for the xanthan solution is interpreted as the usual inertial instability for this geometry, given its dependence on cone angle (not shown).

In figure A-3, both N1 (not shown) and the ratio $N1/\sigma$ increase with shear for the HPAM solution. In marked contrast, for the xanthan solution, the value of $N1/\sigma$ is much lower and shows no increase with shear.

On each transition to increasing stress (Figs. A-2), the viscosity is observed to jump and subsequently fall to a plateau value. Note that the instantaneous viscosity at the plateau is, when the stress is greater than about 1.5 Pa (i.e. in the thickening region for the HPAM solution), significantly noisier for the HPAM solution (Fig A-2 top) than for the xanthan solution (Fig. A-2 bottom), indicative of the presence of elastic fluctuations in the HPAM case.
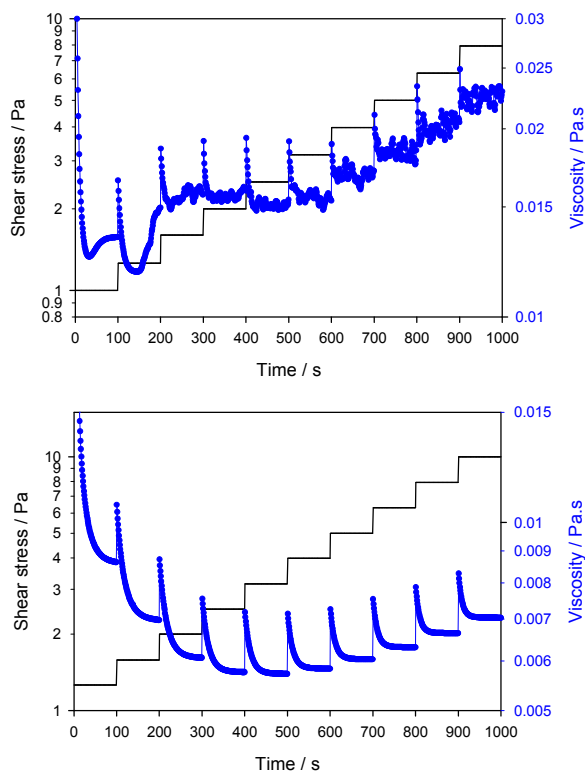

Figure A-2 Top: 0.13wt% HPAM in 74mM brine, instantaneous viscosity (points) on shearing at a series of shear stresses (line), each for 100s.. Bottom: 0.13wt% xanthan in 74mM brine, instantaneous viscosity (points) on shearing at a series of shear stresses (line), each for 100s.
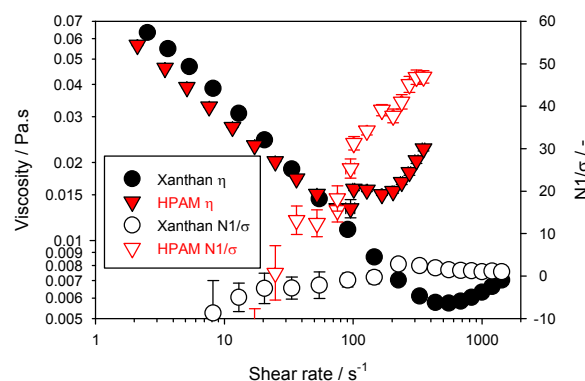

Figure A-3 Viscosity (filled) and ration of N_1 to shear stress (open) for 0.13wt% HPAM (triangles) and 0.13wt% xanthan (circles) in 74mM brine.

From these data we may draw the conclusion that, at low shear-rate, the solutions are similar although the linear viscoelastic relaxation time for the HPAM solution is approximately 3× longer than that for the xanthan solution. However, the behaviour in the non-linear region, i.e. at higher shear and particularly from the point at which the viscosity deviates from power-law thinning, is completely different in nature for the two solutions. The HPAM solution develops a significant first normal stress difference and the flow even in this cone-plate geometry starts to fluctuate. The xanthan

solution does not develop any significant first normal stress difference, even at 20x higher rates than the onset of thickening in the HPAM solution. Moreover the flow in the xanthan solution is much steadier over all rates assessed.

If we take the ratio N1/σ to be a measure of the Weissenberg number describing the solution elasticity (Wi = N1/2σ for the upper convected Maxwell model), then in the shear conditions shown here, the value for HPAM increases from 10 to 50 in the thickening region while for the xanthan solution the value is, within experimental error, barely distinguishable from zero.

Thus we conclude that for these (entangled) solutions the linear viscoelastic response, which is expected to derive from deformation of the entanglements within each system, is comparable. However, under sufficiently strong deformations where we might expect entanglements to be disrupted and molecular relaxation to be dominant, the HPAM solution exhibits strong normal forces whereas the xanthan solution does not. Hence we describe the HPAM solution as significantly more viscoelastic than the xanthan solution.

Notes and references

1. A. F. Morais, H. Seybold, H. J. Hermann and J. S. Andrade, *Physical Review Letters*, 2009, **103**, 194502.
2. M. Brust, C. Schaefer, R. Doerr, L. Pan, M. Garcia, P. E. Arratia and C. Wagner, *Physical Review Letters*, 2013, **110**, 078305.
3. A. Clarke, A. M. Howe, J. Mitchell, J. Staniland, L. Hawkes and K. Leeper, *Soft Matter*, 2015, **11**, 3536-3541.
4. F. Gritti, A. Cavazzini, N. Marchetti and G. Guiochon, *J. Chromatography A*, 2007, **1157**, 289-303.
5. J. S. Andrade Jr, U. M. S. Costa, M. P. Almeida, H. A. Makse and H. E. Stanley, *Physical Review Letters*, 1999, **82**, 5249-5252.
6. J. Bear, *Dynamics of Fluids in Porous Media*, Dover, New York, 1988.
7. K. T. Tallakstad, H. A. Knudsen, T. Ramstad, G. Lovoll, K. J. Maloy, R. Toussaint and E. G. Fikkoy, *Physical Review Letters*, 2009, **102**, 074502.
8. K. S. Lackner, *Science*, 2003, **300**, 1677-1678.
9. L. W. Lake, *Enhanced Oil Recovery*, Prentice-Hall, 1989.
10. S. S. Datta, T. S. Ramakrishnan and D. A. Weitz, *Physics of Fluids*, 2014, **26**, 022002.
11. J. Beaumont, H. Bodiguel and A. Colin, *Soft Matter*, 2013, **9**, 10174-10185.
12. K. S. Sorbie, *Polymer-improved oil recovery*, Springer Science + Business Media, New York, 1991.
13. H. Z. Dong, S. F. Fang, D. M. Wang, J. Y. Wang, Z. Liu and W. H. Hong, *SPE*, 2008, Paper 114342 presented at the SPE/DOE Improved Oil Recovery Symposium held in Tulsa, Oklahoma, USA, 114319-114323 April.
14. D. Wang, J. Cheng, W. Gong, Q. Yang, Q. Li and F. Chen, *SPE*, 2000, Paper 63227 presented at the SPE Annual Technical Conference and Exhibition held in Dallas, Texas, USA, 63221-63224 October.
15. D. Wang, H. Xia, S. Yang and G. Wang, *SPE*, 2010, Paper 127453 presented at the SPE EOR Conference at Oil & Gas West Asia held in Muscat, Omen, 127411-127413 April.
16. A. M. Howe, A. Clarke and D. Giernalczyk, *Soft Matter*, 2015, **11**, 6419-6431.
17. A. Groisman and V. Steinberg, *Nature*, 2000, **405**, 53.
18. J. Mitchell, A. M. Howe and A. Clarke, *J. Magn. Reson.*, 2015, **256**, 34-42.
19. W. S. Price, *Concept. Magn. Reson.*, 1997, **9A**, 299-336.
20. R. S. Seright, T. Fan, K. Wavrik and R. de Carvalho Balaban, *SPE*, 2011, Paper 129200 presented at the SPE Improved Oil Recovery Symposium, 129224-129228 april, Tulsa, Oklahoma, USA.
21. P. Pakdel and G. H. McKinley, *Physical Review Letters*, 1996, **77**, 2459-2462.
22. R. M. Cotts, M. J. R. Hoch, T. Sun and J. T. Markert, *Journal of Magnetic Resonance*, 1989, **83**, 252-266.
23. G. Leu, E. J. Fordham, M. D. Hurlimann and P. Frulla, *Magnetic Resonance Imaging*, 2005, **23**, 305-309.
24. J. E. Tanner, *Journal of Chemical Physics*, 1970, **52**, 2523-2526.
25. W. S. Price, *Concept. Magn. Reson.*, 1998, **10A**, 197-237.
26. F. Walther, T. Drobek, A. M. Gigler, M. Hennemeyer, M. Kaiser, H. Herberg, T. Shimitsu, G. E. Morfill and R. W. Stark, *Surf. Interf. Anal.*, 2010, **42**, 1735-1744.
27. A. Groisman and V. Steinberg, *New Journal of Physics*, 2004, **6**, 29-29.
28. M. D. Hurlimann, L. Venkataramanan and C. Flaum, *J. Chem. Phys.*, 2002, **117**, 10223-10232.
29. J. E. Tanner and E. O. Stejskal, *Journal of Chemical Physics*, 1968, **49**, 1768-1777.
30. D. J. Holland, J. Mitchell, A. Blake and L. F. Gladden, *Phys. Rev. Lett.*, 2013, **110**.
31. R. T. Armstrong, A. Georgiadis, H. Ott, D. Klemin and S. Berg, *Geophys. Res. Lett.*, 2014, **41**, 55-60.
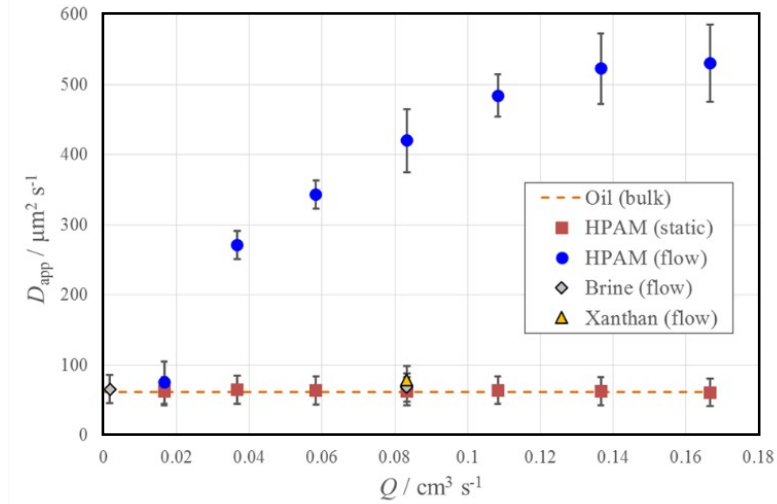
NMR measurement of anomalous diffusion has been used to detect trapped oil-ganglia fluctuations in a complex porous 3D system.